

Proximity-induced Rashba spin-orbit interaction in BaMnO₃|KTaO₃ heterostructure for antiferromagnetic spintronics

Vivek Kumar and Nirmal Ganguli*

Department of Physics, *Indian Institute of Science Education and Research Bhopal, Bhauri, Bhopal 462066, India*

(Dated: 11 August 2025)

Antiferromagnetic spintronics, a promising technology for ultra-fast electronic devices, faces several challenges, including the lack of materials simultaneously hosting robust antiferromagnetism and adequate Rashba-like interaction. We design a heterostructure of BaMnO₃|KTaO₃ with the idea of proximity-inducing strong Rashba spin-orbit interaction from KTaO₃ part to BaMnO₃ part, where the latter is already a robust antiferromagnet. Within our DFT calculations, the heterostructure reveals BaMnO₃ bands near the Fermi level with a significant magnetic moment per Mn atom and a decent ordering temperature. Further, the BaMnO₃ bands in the heterostructure exhibit linear Rashba interaction with a sizable Rashba coefficient, owing to its proximity to KTaO₃. Our work can motivate future research by demonstrating the road map to proximity-induced Rashba interaction for antiferromagnetic spintronics.

Spin-orbit interaction (SOI) partnered with inversion asymmetry is known to result in spin splitting and helical spin textures that may help realize tunable spin-orbit torque, a key to antiferromagnetic spintronics [1]. However, simultaneously realizing robust antiferromagnetism and strong SOI has been a challenge, slowing the progress in this area. Oxide heterostructures host several attractive features ranging from a two-dimensional electron system to magnetism and Rashba interaction [2–9], making them excellent testbeds for future technology. Zhong *et al.* [6] predicted a Rashba interaction in LaAlO₃|SrTiO₃ heterostructure, for which Lin *et al.* [10] estimated a weak Rashba coefficient. KTaO₃ (KTO) (001) surface shows a giant Rashba splitting [9, 11–15], although it hosts no magnetism. Earlier, we designed and simulated a heterostructure of LaAlO₃|SrIrO₃|SrTiO₃ to be a suitable platform for antiferromagnetic spintronics [7, 16], where we observed strong Rashba-Dresselhaus interaction, although a weak antiferromagnetism with a small magnetic moment coming from the Ir-5*d* states.

We propose an oxide heterostructure to find an optimum solution to this problem using proximity effect, where some features of one component of a heterostructure, including magnetism, superconductivity, and spin-orbit interaction, can be induced to the other component, making the heterostructure host features far more promising for technology than the collection of the individual components' features [17–25]. In an earlier work on LaAlO₃|SrIrO₃|SrTiO₃ heterostructure, we observed stronger than usual spin splitting of the Ti-3*d* states besides a strong Rashba-Dresselhaus interaction in the Ir-5*d* states [7]. Motivated by this observation, here we consider a heterostructure of KTO, a perovskite oxide showing strong Rashba interaction owing to Ta-5*d* states, with BaMnO₃ (BMO), a robust antiferromagnet owing to the Mn-3*d* states. Although most stable in a hexagonal structure [26], a cubic phase of BMO can be realized [27, 28].

Thus, when grown on a thick substrate of cubic KTO, BMO is expected to grow in a cubic phase with a reasonable lattice match [29].

In this Letter, we demonstrate through our simulations on a reasonable and computationally tractable BMO|KTO heterostructure that an antiferromagnetic BMO component may be realized with a decent ordering temperature and the heterostructure bands aligning in such a way that both the valence band top and the conduction band bottom correspond to the BMO part due to the electrostatic potential development, as discussed below. Further, our calculations reveal that a reasonably strong Rashba spin-orbit interaction can be induced in the BMO part, paving the way to overcome many pragmatic challenges for technology based on antiferromagnetic spintronics.

We simulate a heterostructure with a periodically repeated supercell comprising three unit cell thick KTO and two unit cell thick BMO perpendicular to the interface, henceforth denoted as the (BaMnO₃)₂|(KTaO₃)₃ heterostructure. Assuming epitaxial growth of BMO on a thick substrate of KTO, we fix the heterostructure's in-plane lattice constant to 3.988 Å matching that of KTO [30], and allow optimization for the lattice constant along the *c*-direction. We employed density functional theory as implemented in the VASP code [31, 32] for the total energy, electronic structure, and magnetic properties calculations. Spin-orbit interaction (SOI) is considered for all calculations except structure optimization. Local spin density approximation (LSDA) [33, 34] with Hubbard-*U* correction [35] for strong electron-electron correction with $U_{\text{eff}} = U - J = 1$ and 3 eV for Ta-5*d* and Mn-3*d* states, respectively, is employed for describing the exchange-correlation functional. The projector augmented wave (PAW) method [36], combined with a plane wave basis set with a cutoff energy of 450 eV, describes the potential and expands the wavefunctions. The Brillouin zone integrations are performed using the improved tetrahedron method [37] over a Γ -centered $11 \times 11 \times 1$ *k*-point mesh. A small energy threshold of 10^{-7} eV is used for self-consistent calculations considering SOI.

* Contact author: NGanguli@iiserb.ac.in

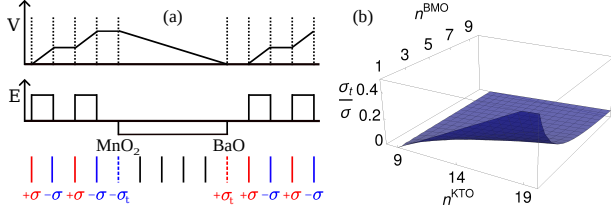


FIG. 1. The electric field E and the electrostatic potential energy V due to the BMO|KTO superlattice are illustrated in (a) for the alternating $+1|-1$ charged planes in KTO and neutral planes in BMO, assuming a parallel plate capacitor model. The required charge transfer with increasing thickness of BMO and KTO layers is displayed in (b).

The atomic positions are optimized by minimizing the Hellman-Feynman forces on each atom to a tolerance of 10^{-2} eVÅ $^{-1}$.

The heterojunction between a polar and a nonpolar material experiences a charge transfer that plays a crucial role in its electronic properties. While the mechanism of charge transfer at perovskite oxide heterojunctions is debated, the electrostatic origin of the phenomenon is established [3, 9]. Being a heterostructure of a nonpolar and a polar material, the electrostatic potential in BMO|KTO heterostructure will show similar patterns as other oxide heterostructures [3]. If a film of BMO is deposited on a thick KTO substrate, the electrostatic potential development may be described similarly to Refs. [3, 9]. However, the BMO|KTO superlattice considered here is distinct in its geometry; therefore, it calls for a compatible theoretical model describing the electrostatic potential. As illustrated in Fig. 1(a) (bottom panel), we consider n^{KTO} number of KTO unit cells, followed by n^{BMO} number of BMO unit cells, and the arrangement repeats itself within periodic boundary conditions. Considering a heterostructure of the (001) planes, a KTO unit cell nominally comprises a $(\text{Ta}^{5+}\text{O}_2^{2-})^+$ plane and a $(\text{K}^+\text{O}^{2-})^-$ plane, resulting in an alternating arrangement of planes with $+\sigma$ and $-\sigma$ surface charge densities. On the other hand, a BMO unit cell nominally comprises a $(\text{Mn}^{4+}\text{O}_2^{2-})^0$ plane and a $(\text{Ba}^{2+}\text{O}_2^{2-})^0$ plane, both being charge neutral. The arrangement yields two heterojunctions: one between $(\text{KO})^-$ and $(\text{MnO}_2)^0$ planes, and the other between $(\text{BaO})^0$ and $(\text{TaO}_2)^+$ planes, as illustrated in Fig. 1(a). The corresponding electrostatic potential energy would diverge for a large thickness of the constituent films, unless some charge transfer takes place to the MnO_2 and the BaO planes at the interfaces, leading to $-\sigma_t$ and $+\sigma_t$ surface charge densities, respectively, to contain the potential within a threshold value V_{Th} . As our calculations reveal a type-I band alignment where the valence band maximum and the conduction band minimum of the smaller band gap material BMO lies within the band gap of KTO, we expect the threshold potential V_{Th} to be the sum of BMO's band gap ϵ_g^{BMO} and the valence band

offset Δ .

$$V_{\text{Th}} = \epsilon_g^{\text{BMO}} + \Delta \geq \frac{n^{\text{KTO}} a^{\text{KTO}} \sigma}{2\epsilon^{\text{KTO}}} - \frac{n^{\text{BMO}} a^{\text{BMO}} \sigma_t}{\epsilon^{\text{BMO}}}, \quad (1)$$

where ϵ^{KTO} and ϵ^{BMO} are the permittivity of KTO and BMO, respectively, while a^{KTO} and a^{BMO} denote the inter-planar distance in KTO and BMO parts of the heterostructure. The first term in the right-hand side of Eq. (1) corresponds to the uprising lines in the potential energy in the KTO part (see Fig. 1(a)), while the second term represents the downward line in the BMO part. We may express the ratio of transferred surface charge density to the KTO surface charge density as

$$\frac{\sigma_t}{\sigma} \geq \frac{\epsilon^{\text{BMO}}}{n^{\text{BMO}} a^{\text{BMO}}} \left(\frac{n^{\text{KTO}} a^{\text{KTO}}}{2\epsilon^{\text{KTO}}} - \frac{V_{\text{Th}}}{\sigma} \right). \quad (2)$$

The model suggests that a charge transfer to the interface is required for

$$n^{\text{KTO}} > \frac{2\epsilon^{\text{KTO}} V_{\text{Th}}}{a^{\text{KTO}} \sigma}. \quad (3)$$

We gather from Eqs. (2) and (3) that the onset of charge transfer at the interface depends only on the KTO thickness in the superlattice. In contrast, BMO thickness impacts the amount of charge transfer once the onset condition is met. Using a set of reasonable parameter values [38], we estimate that 10 unit cell 10-unit-cell-thick KTO is required for the onset of a charge transfer. Figure 1(b) displays the ratio of transferred surface charge density to the value of surface charge density in KO or TaO_2 planes as a function of the KTO and BMO thickness, illustrating the charge transfer landscape in the system. The figure suggests a required onset of charge transfer with at least 10 unit cell thick KTO and more charge transfer with increasing KTO thickness, while a thicker BMO layer would attenuate the charge transfer. However, unlike the KTaO_3 slab [9] or $\text{LaAlO}_3|\text{SrTiO}_3$ heterostructure [3], Eq. (2) does not suggest any asymptotic limit for σ_t/σ in this superlattice; the ratio monotonically increases with increasing KTO thickness. Simulating different antiferromagnetic arrangements requires a $2a \times 2b$ in-plane breadth. To make our calculations tractable, we limit the thickness of BMO and KTO layers to 2 and 3 unit cells, respectively. Although the above discussion does not warrant a charge transfer in this limit, we can investigate the crucial magnetic properties and Rashba interaction within this computationally tractable simulation cell.

We start with simulating a $2a \times 2b$ cell for $(\text{BaMnO}_3)_2|(\text{KTaO}_3)_3$ heterostructure within periodic boundary conditions, leading to a supercell arrangement. Unlike in Ref. [16], here we choose an inversion-asymmetric structure to allow for the possibility of Rashba-like interaction in the absence of any structural distortion. The band structure and the density of states (DoS) calculated within spin-orbit interaction, displayed in Fig. 2(a) and Fig. 2(b), indicate a gap of ~ 0.65 eV

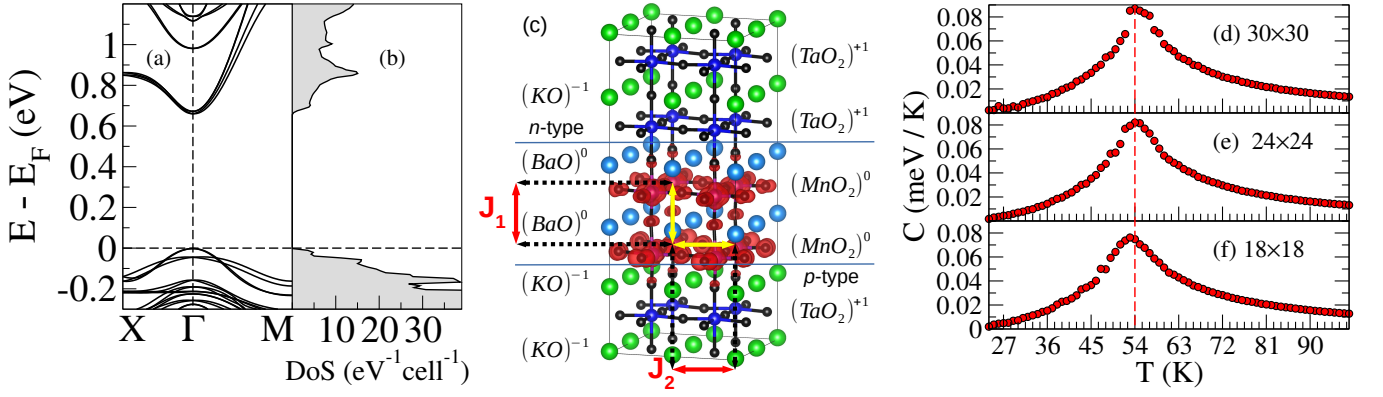


FIG. 2. The band structure of $(\text{BaMnO}_3)_2|(\text{KTaO}_3)_3$ superlattice along $X \rightarrow \Gamma \rightarrow M$ direction including spin-orbit interaction for C-type antiferromagnetic arrangement with spin quantization along (001) direction is shown in (a), while (b) shows the corresponding density of states. (c) shows the partial charge density corresponding to the bands near the Fermi level, confirming their mapping onto the BaMnO_3 part. The VESTA software has been used for preparing panel (c) [39]. The variation of magnetic specific heat as a function of temperature is shown for lattice sizes (d) 30×30 , (e) 24×24 , and (f) 18×18 within periodic boundary conditions.

TABLE I. The energy difference per Mn atom, spin moment, and orbital moment at Mn sites obtained from our DFT calculations within LSDA + SOC + $U_{\text{eff}} = 3$ eV for different magnetic arrangements and (001) spin-quantization axis are tabulated here.

Arrangement	Energy (meV)	Spin (orbital) moment (μ_B)
C-type AFM	0.0	2.776 (0.028)
FM	33.7	3.011 (0.027)
A-type AFM	34.5	2.981 (0.028)
G-type AFM	57.8	2.815 (0.028)

TABLE II. The exchange interaction strengths estimated from our calculations are listed here.

Exchange path	Distance (\AA)	Strength (meV)
J_1	3.77	4.96
J_2	3.99	-1.86

between the valence and the conduction bands for the superlattice of our choice, with all bands close to the Fermi level (below and above) corresponding to the BMO part, as seen from the projected charge density in Fig. 2(c). The interface can be made a conducting one by increasing the KTO layer thickness, as indicated in Eq. (2). Our test calculation with $(\text{BaMnO}_3)_2|(\text{KTaO}_3)_{20}$ heterostructure reveals a conducting interface. Although the $(\text{BaMnO}_3)_2|(\text{KTaO}_3)_3$ heterostructure does not host a conducting interface desired for antiferromagnetic spintronics, we continue further calculations with this heterostructure, as we obtain invaluable insights about the spin-orbit interaction within an affordable computational cost that would be equally valid for a heterostructure with a conducting interface.

In order to find the lowest-energy magnetic configuration, we simulated A-type, C-type, and G-type antifer-

romagnetic (AFM) arrangements in the BaMnO_3 part, besides simulating the ferromagnetic (FM) arrangement. Our results, summarized in Table I, reveal the C-type antiferromagnetic arrangement to have the lowest energy.

We estimate the strengths of the magnetic exchange interactions by mapping our DFT results onto a spin Hamiltonian

$$H = - \sum_{i,j} J_{ij} \vec{S}_i \cdot \vec{S}_j, \quad (4)$$

with \vec{S} denoting the spin vector and i, j representing spins and site indices, respectively, can be determined by examining the relative energies of the C-, G-, and A-type magnetic configurations. The exchange interaction strengths along two different directions are referred to as J_1 (out-of-plane) and J_2 (in-plane) (see Fig. 2(c)). The interaction strengths are estimated and presented in Table II.

The magnetic ordering temperature, also known as the Néel temperature in antiferromagnets, can be estimated using the exchange interaction strengths listed in Table I. The magnetic specific heat C is estimated as

$$C = \frac{1}{N} \frac{\partial U}{\partial T} = \frac{\langle \varepsilon^2 \rangle - \langle \varepsilon \rangle^2}{N k_B T^2}, \quad (5)$$

where ε , N , k_B , and T represent the energy of each magnetic configuration, the number of spins, the Boltzmann constant, and the temperature, respectively. $U(T) = \langle \varepsilon \rangle$ is the average internal energy. The energy of the magnetic configurations in the heterostructure with collinear spins and limited periodicity in the c -direction is given by

$$\varepsilon = -J_1 \sum_{i,j} S_i S_j - J_2 \sum_{i,k=1}^{k=4} S_i S_k, \quad (6)$$

where i, j iterate over the atoms satisfying the distance of the corresponding exchange path J_1 or J_2 . In our calculations, we consider three different lattice sizes $30 \times 30, 24 \times 24$, and 18×18 within periodic boundary conditions. We employ the Metropolis Monte Carlo simulation algorithm to calculate $\langle \varepsilon^2 \rangle$ and $\langle \varepsilon \rangle$ at different temperatures. A spin S_i is randomly chosen from the lattice, and the energy cost $\Delta \varepsilon$ for flipping the spin is computed. The flip is accepted if the corresponding Boltzmann weight, $\exp(-\Delta \varepsilon/k_B T)$, is greater than a random number $r \in (0, 1)$. Another spin is randomly selected in the next time step. We average over 10^8 imaginary time steps after bringing the system to thermal equilibrium in 10^9 imaginary time steps for each temperature considered here. The results, shown in Fig. 2(d), 2(e), and 2(f) for the $18 \times 18, 24 \times 24$ and 30×30 , respectively, within periodic boundary conditions, indicate an ordering temperature of ~ 54 K – a sizable value for an antiferromagnet with restricted interactions.

Although our calculation reveals no Rashba splitting for inversion-symmetric bulk BaMnO₃ in the cubic structure and a slab of BaMnO₃ with broken structure inversion symmetry, the band dispersion for the (BaMnO₃)₂|(KTaO₃)₃ heterostructure, displayed in Fig. 3(a) and Fig. 3(b), exhibits pronounced Rashba-like splitting of bands. A projected charge-density isosurface plot shown in Fig. 2(c) maps the Rashba-split bands near the Fermi level to the BaMnO₃ part of the heterostructure. While KTaO₃ is known to host strong spin-orbit interaction and a KTaO₃ slab exhibits strong Rashba splitting [9], our observation of pronounced Rashba-like splitting in the BaMnO₃ part suggests proximity-induced spin-orbit interaction at the BaMnO₃ part. We further analyze the orbital characters of the Rashba-split bands near the Fermi level, as seen in Fig. 3(c), 3(d), 3(e), and 3(f) representing the orbital characters of Mn d_{xy} , Mn d_{yz} , Mn d_{zx} , Mn $d_{x^2-y^2}$, O p_y , and Ta d_{xy} , respectively, suggesting a clear dominance of Mn d orbitals in the valence and the conduction bands. The highly dispersive valence band maximum corresponds to O p_y orbitals. The Ta- d orbitals exhibit their presence at an elevated energy in the conduction bands, establishing a proximity-induced Rashba-like splitting in the BaMnO₃ part of the heterostructure.

After ascertaining that the proximity of Ta 5d orbitals with strong spin-orbit interaction induces substantial spin-orbit interaction in Mn 3d orbitals, we examine the exact nature of the Rashba-like interaction in the system. Focusing on three pairs of bands near the valence band maximum, we plot the corresponding 3D band dispersion $\varepsilon(k_x, k_y)$, their cross-sections, and the corresponding spin textures, where each spin vector is represented as $\vec{S} = \hat{x}\langle\psi|\hat{S}_x|\psi\rangle_{\vec{k}} + \hat{y}\langle\psi|\hat{S}_y|\psi\rangle_{\vec{k}}$, where $|\psi\rangle$ is the DFT-obtained electronic state, combined with isoenergetic contours, as displayed in Fig. 4. Figure 4(a) and 4(b) visualize the pair of bands and their cross-section, respectively, at the top of the valence bands near the Γ -point in 3D, clearly illustrating the splitting pat-

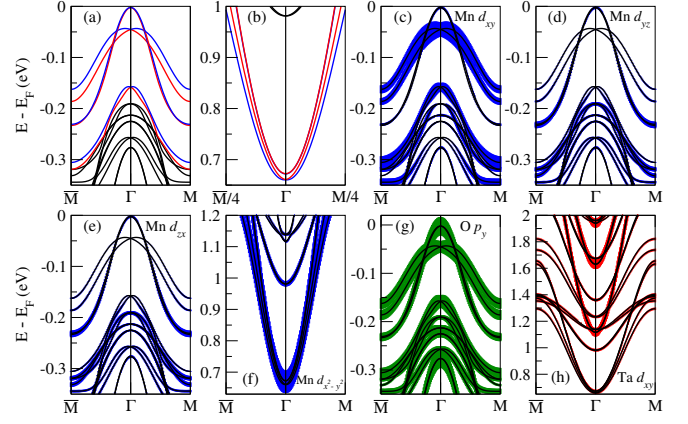


FIG. 3. The spin-split bands of the (BaMnO₃)₂|(KTaO₃)₃ heterostructure along $\bar{M} \rightarrow \Gamma \rightarrow M$ below and above the Fermi level have been highlighted in (a) and (b), respectively, exhibiting Rashba splitting. The orbital characters of the Rashba-split bands near the Fermi level of the heterostructure are highlighted, with Mn d_{xy} , Mn d_{yz} , Mn d_{zx} , Mn $d_{x^2-y^2}$, O p_y , and Ta d_{xy} orbital characters featuring in (c), (d), (e), (f), (g), and (h), respectively.

tern. The corresponding helical spin textures, shown in Fig. 4(c) and 4(d), reveal the spins rotating along the bands' isoenergetic contours, resembling linear Rashba interaction [9, 16]. The second and third pair of valence bands near the Γ -point exhibit a similar pattern of linear Rashba splitting and spin texture, as seen in Fig. 4(e-h) and Fig. 4(i-l), respectively. The second pair of bands obtained from our DFT calculations may be reasonably fitted to a two-band Rashba model with the effective mass $m^* = -0.49m_e$ and the linear Rashba coefficient $\alpha_{(1)} = 0.063$ eVÅ, while the third pair fits to $m^* = -0.402m_e$ and $\alpha_{(1)} = 0.114$ eVÅ, m_e being the electron's mass. Thus, our results show the induced spin-orbit interaction on the hybridized Mn and O bands near the Fermi level to be predominantly linear Rashba interaction. The negative signs in the effective mass indicate the usual convex upwards pattern of the valence bands near the Γ -point.

The above discussion calls for a comparison of the induced linear Rashba coefficient $\alpha_{(1)}$ from Mn bands with that of the KTaO₃ surface and LaAlO₃|SrTiO₃ heterostructure. The Rashba coefficient calculated by Varotto *et al.* [11] and Zhang *et al.* [40] is approximately 0.31 eVÅ at KTaO₃ interfaces. The Rashba coefficient estimated here for the Mn-3d_{xy} states in the BMO|KTO heterostructure is approximately four times larger than that found in the LaAlO₃|SrTiO₃ interface, as reported by Lin *et al.* [10], establishing the usefulness of proximity-induced SOI for the manifestation of strong Rashba interaction in the BMO part of the BMO|KTO heterostructure.

In summary, we simulate a heterostructure of BaMnO₃|KTaO₃ with the view of combining a robust antiferromagnet and a strong spin-orbit interaction ma-

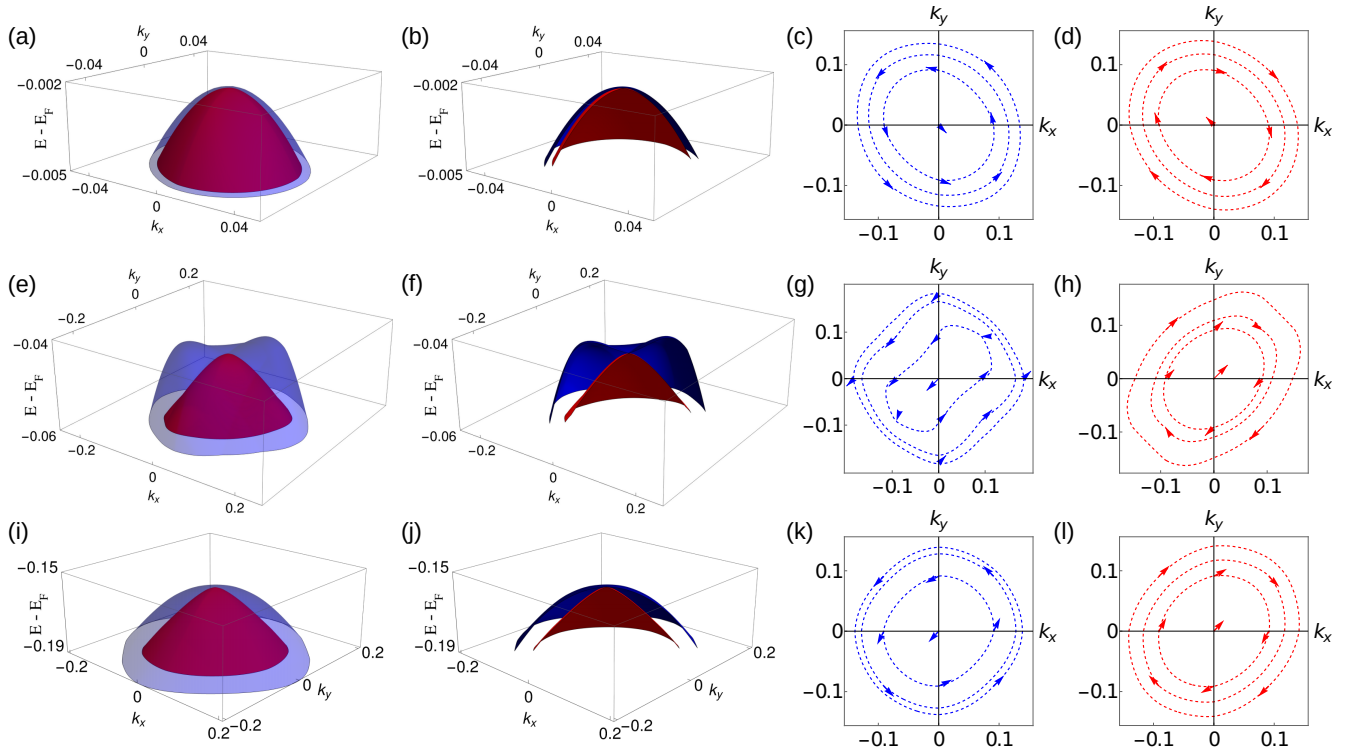


FIG. 4. The Rashba-like split bands near the Fermi energy are closely visualized here with the help of three-dimensional (3D) bands, band cross sections, and spin textures. The 3D bands and their cross-section for the pair of bands at the valence band maximum (see Fig. 2(c)) are visualized in (a) and (b), while the corresponding spin textures are shown in (c) and (d) on multiple isoenergetic contours. Similarly, the 3D bands and their cross-section for the pair of bands right below the valence band maximum at the Γ -point (see Fig. 2(c)) are shown in (e) and (f), with the corresponding spin textures on multiple isoenergetic contours in (g) and (h). Finally, (i) and (j) show the 3D bands and their cross-section for the third highest pair of valence bands highlighted in Fig. 3(a), with the corresponding spin textures on multiple isoenergetic contours in (k) and (l).

terial to realize a heterostructure useful for antiferromagnetic spintronics. The electrostatic potential developed in the superlattice due to a combination of polar/nonpolar materials result in BMO bands near the Fermi level and an onset of charge transfer beyond 10 unit cell thick KTO layer. The BMO part in the heterostructure shows strong antiferromagnetism with significant magnetic moment at the Mn sites and reasonably strong interactions leading to an ordering temperature of at least 54 K. Our results confirm the induction of a reasonably strong spin-orbit interaction in the BMO part due to its proximity to the KTO part, resulting in a substantial linear Rashba coefficient. Thus, based on our estimation of electrostatic potential, DFT calculations, and Monte Carlo simula-

tions, we demonstrate the BMO|KTO heterostructure to offer a combination of reasonably strong antiferromagnetism and Rashba spin-orbit interaction – a lucrative combination of features for antiferromagnetic spintronics – owing to the proximity effect. Besides, the idea of designing heterostructures for proximity-induced features can motivate future theoretical and experimental works.

Fruitful scientific discussion with Dr. Jayita Chakraborty, financial support from SERB, India, through grant numbers CRG/2021/005320 and ECR/2016/001004, and the use of a high-performance computing facility at IISER Bhopal are gratefully acknowledged.

-
- [1] V. Baltz, A. Manchon, M. Tsoi, T. Moriyama, T. Ono, and Y. Tserkovnyak, Antiferromagnetic spintronics, *Rev. Mod. Phys.* **90**, 015005 (2018).
 - [2] A. Ohtomo and H. Y. Hwang, A high-mobility electron gas at the $\text{LaAlO}_3/\text{SrTiO}_3$ heterointerface, *Nature* **427**, 423 (2004).
 - [3] N. Ganguli and P. J. Kelly, Tuning Ferromagnetism at

- Interfaces between Insulating Perovskite Oxides, *Phys. Rev. Lett.* **113**, 127201 (2014).
- [4] J. A. Bert, B. Kalisky, C. Bell, M. Kim, Y. Hikita, H. Y. Hwang, and K. A. Moler, Direct imaging of the coexistence of ferromagnetism and superconductivity at the $\text{LaAlO}_3/\text{SrTiO}_3$ interface, *Nat. Phys.* **7**, 767 (2011).
- [5] L. Li, C. Richter, J. Mannhart, and R. C. Ashoori, Co-

- existence of magnetic order and two-dimensional superconductivity at $\text{LaAlO}_3/\text{SrTiO}_3$ interfaces, *Nat. Phys.* **7**, 762 (2011).
- [6] Z. Zhong, A. Tóth, and K. Held, Theory of spin-orbit coupling at $\text{LaAlO}_3/\text{SrTiO}_3$ interfaces and SrTiO_3 surfaces, *Phys. Rev. B* **87**, 161102 (2013).
- [7] J. Chakraborty and N. Ganguli, Perovskite oxide heterojunction for Rashba-Dresselhaus assisted antiferromagnetic spintronics, *Phys. Rev. B* **102**, 214425 (2020).
- [8] L. M. Vicente-Arche, J. Bréhin, S. Varotto, M. Cosset-Cheneau, S. Mallik, R. Salazar, P. Noël, D. C. Vaz, F. Trier, S. Bhattacharya, A. Sander, P. Le Fèvre, F. Bertran, G. Saiz, G. Ménard, N. Bergeal, A. Barthélémy, H. Li, C. Lin, D. E. Nikonov, I. A. Young, J. E. Rault, L. Vila, J. Attané, and M. Bibes, Spin-Charge Interconversion in KTaO_3 2D Electron Gases, *Adv. Mater.* **33**, 2102102 (2021).
- [9] V. Kumar and N. Ganguli, Rashba-like spin-orbit interaction and spin texture at the $\text{KTaO}_3(001)$ surface from DFT calculations, *Phys. Rev. B* **106**, 125127 (2022).
- [10] W. Lin, L. Li, F. Doğan, C. Li, H. Rotella, X. Yu, B. Zhang, Y. Li, W. S. Lew, S. Wang, W. Prellier, S. J. Pennycook, J. Chen, Z. Zhong, A. Manchon, and T. Wu, Interface-based tuning of Rashba spin-orbit interaction in asymmetric oxide heterostructures with 3d electrons, *Nat. Commun.* **10**, 3052 (2019).
- [11] S. Varotto, A. Johansson, B. Göbel, L. M. Vicente-Arche, S. Mallik, J. Bréhin, R. Salazar, F. Bertran, P. L. Fèvre, N. Bergeal, J. Rault, I. Mertig, and M. Bibes, Direct visualization of Rashba-split bands and spin/orbital-charge interconversion at KTaO_3 interfaces, *Nat. Commun.* **13**, 6165 (2022).
- [12] A. Gupta, H. Silotia, A. Kumari, M. Dumen, S. Goyal, R. Tomar, N. Wadehra, P. Ayyub, and S. Chakraverty, KTaO_3 —The New Kid on the Spintronics Block, *Adv. Mater.* **34**, 2106481 (2022).
- [13] M. Setvin, M. Reticcioli, F. Poelzleitner, J. Hulva, M. Schmid, L. A. Boatner, C. Franchini, and U. Diebold, Polarity compensation mechanisms on the perovskite surface $\text{KTaO}_3(001)$, *Science* **359**, 572 (2018).
- [14] P. Kim, K. T. Kang, G. Go, and J. H. Han, Nature of orbital and spin Rashba coupling in the surface bands of SrTiO_3 and KTaO_3 , *Phys. Rev. B* **90**, 205423 (2014).
- [15] S. K. Ojha, S. K. Gogoi, P. Mandal, S. D. Kaushik, J. W. Freeland, M. Jain, and S. Middey, Oxygen vacancy induced electronic structure modification of KTaO_3 , *Phys. Rev. B* **103**, 085120 (2021).
- [16] N. Ganguli, A. Singh, V. Kumar, and J. Chakraborty, Mapping Rashba and Dresselhaus spin-orbit interactions to inversion asymmetry in perovskite oxide heterostructures, *Phys. Rev. B* **111**, 064413 (2025).
- [17] D. Marchenko, A. Varykhalov, M. Scholz, G. Bihlmayer, E. Rashba, A. Rybkin, A. Shikin, and O. Rader, Giant Rashba splitting in graphene due to hybridization with gold, *Nat. Commun.* **3**, 1232 (2012).
- [18] S. V. Eremeev, V. N. Men'shov, V. V. Tugushev, P. M. Echenique, and E. V. Chulkov, Magnetic proximity effect at the three-dimensional topological insulator/magnetic insulator interface, *Phys. Rev. B* **88**, 144430 (2013).
- [19] A. Avsar, J. Y. Tan, T. Taychatanapat, J. Balakrishnan, G. Koon, Y. Yeo, J. Lahiri, A. Carvalho, A. S. Rodin, E. O'Farrell, G. Eda, A. H. Castro Neto, and B. Özyilmaz, Spin-orbit proximity effect in graphene, *Nat. Commun.* **5**, 4875 (2014).
- [20] Z. Qiao, W. Ren, H. Chen, L. Bellaiche, Z. Zhang, A. H. MacDonald, and Q. Niu, Quantum Anomalous Hall Effect in Graphene Proximity Coupled to an Antiferromagnetic Insulator, *Phys. Rev. Lett.* **112**, 116404 (2014).
- [21] F. Katmis, V. Lauter, F. S. Nogueira, B. A. Assaf, M. E. Jamer, P. Wei, B. Satpati, J. W. Freeland, I. Eremin, D. Heiman, P. Jarillo-Herrero, and J. S. Moodera, A high-temperature ferromagnetic topological insulating phase by proximity coupling, *Nature* **533**, 513 (2016).
- [22] J. O. Island, X. Cui, C. Lewandowski, J. Y. Khoo, E. M. Spanton, H. Zhou, D. Rhodes, J. C. Hone, T. Taniguchi, K. Watanabe, L. S. Levitov, M. P. Zaletel, and A. F. Young, Spin-orbit-driven band inversion in bilayer graphene by the van der Waals proximity effect, *Nature* **571**, 85 (2019).
- [23] S. Tamura and Y. Tanaka, Theory of the proximity effect in two-dimensional unconventional superconductors with Rashba spin-orbit interaction, *Phys. Rev. B* **99**, 184501 (2019).
- [24] Q. Tong, M. Chen, and W. Yao, Magnetic Proximity Effect in a van der Waals Moiré Superlattice, *Phys. Rev. Applied* **12**, 024031 (2019).
- [25] A. López, L. Colmenárez, M. Peralta, F. Mireles, and E. Medina, Proximity-induced spin-orbit effects in graphene on Au, *Phys. Rev. B* **99**, 085411 (2019).
- [26] B. Chamberland, A. Sleight, and J. Weiher, Preparation and characterization of BaMnO_3 and SrMnO_3 polytypes, *Journal of Solid State Chemistry* **1**, 506 (1970).
- [27] P. S. Dobal, A. Dixit, R. S. Katiyar, Z. Yu, R. Guo, and A. S. Bhalla, Micro-Raman scattering and dielectric investigations of phase transition behavior in the BaTiO_3 - BaZrO_3 system, *J. Appl. Phys.* **89**, 8085 (2001).
- [28] G. Gökoğlu and H. Yildirim, Electronic structure and surface properties of cubic perovskite oxide BaMnO_3 , *Computational Materials Science* **50**, 1212 (2011).
- [29] R. Søndena, S. Stølen, P. Ravindran, T. Grande, and N. L. Allan, Corner- versus face-sharing octahedra in AMnO_3 perovskites ($A = \text{Ca}, \text{Sr}, \text{and Ba}$), *Phys. Rev. B* **75**, 184105 (2007).
- [30] J. B. Goodenough and M. Longo, 3.1.7 Data: Crystallographic properties of compounds with perovskite or perovskite-related structure, in *Landolt-Börnstein - Group III Condensed Matter* (Springer-Verlag, Berlin/Heidelberg, 1970) pp. 148–161.
- [31] G. Kresse and J. Furthmüller, Efficient iterative schemes for ab initio total-energy calculations using a plane-wave basis set, *Phys. Rev. B* **54**, 11169 (1996).
- [32] G. Kresse and D. Joubert, From ultrasoft pseudopotentials to the projector augmented-wave method, *Phys. Rev. B* **59**, 1758 (1999).
- [33] D. M. Ceperley and B. J. Alder, Ground State of the Electron Gas by a Stochastic Method, *Phys. Rev. Lett.* **45**, 566 (1980).
- [34] J. P. Perdew and A. Zunger, Self-interaction correction to density-functional approximations for many-electron systems, *Phys. Rev. B* **23**, 5048 (1981).
- [35] S. L. Dudarev, G. A. Botton, S. Y. Savrasov, C. J. Humphreys, and A. P. Sutton, Electron-energy-loss spectra and the structural stability of nickel oxide: An LSDA+U study, *Phys. Rev. B* **57**, 1505 (1998).
- [36] P. E. Blöchl, Projector augmented-wave method, *Phys. Rev. B* **50**, 17953 (1994).
- [37] P. E. Blöchl, O. Jepsen, and O. K. Andersen, Improved tetrahedron method for Brillouin-zone integra-

- tions, [Phys. Rev. B **49**, 16223 \(1994\)](#).
- [38] We use $\epsilon^{\text{KTO}} = 220\epsilon_0$ [41], ϵ_0 being the free-space permittivity, $\epsilon^{\text{BMO}} = 22\epsilon_0$ [42], $\epsilon_g^{\text{BMO}} = 1.08$ eV [28], $\Delta = -0.145$ eV, and $a^{\text{KTO}} = 3.988$ Å for the calculations.
- [39] K. Momma and F. Izumi, VESTA 3 for three-dimensional visualization of crystal, volumetric and morphology data, [J. Appl. Cryst. **44**, 1272 \(2011\)](#).
- [40] H. Zhang, X. Yan, X. Zhang, S. Wang, C. Xiong, H. Zhang, S. Qi, J. Zhang, F. Han, N. Wu, B. Liu, Y. Chen, B. Shen, and J. Sun, Unusual Electric and Optical Tuning of KTaO_3 -Based Two-Dimensional Electron Gases with 5d Orbitals, [ACS Nano **13**, 609 \(2019\)](#).
- [41] M. D. Agrawal and K. V. Rao, Dielectric properties and optical absorption of KTaO_3 single crystals and $\text{KTaO}_3\text{NaTaO}$ mixed crystals, [J. Phys. C: Solid State Phys. **3**, 1120 \(1970\)](#).
- [42] L. Hughes, A. Roy, N. Yadav, C. Downing, M. P. Browne, J. K. Vij, and V. Nicolosi, Dielectric Engineering of Perovskite BaMnO_3 for the Rapid Heterogeneous Nucleation of Pt Nanoparticles for Catalytic Applications, [Advanced Functional Materials **34**, 2402103 \(2024\)](#).